Structure–Property Relationships in Redox-Derivatized Metal–Insulator–Semiconductor (MIS) Photoanodes

Ponart Aroonratsameruang, Pichaya Pattanasattayavong, Vincent Dorcet, Cristelle Mériadec, Soraya Ababou-Girard, Stéphanie Fryars, Gabriel Loget

Structure-property Relationships in Redox-Derivatized Metal-Insulator-Semiconductor (MIS) Photoanodes

Ponart Aroonratsameruang,[‡,†] *Pichaya Pattanasattayavong,*[†,§] *Vincent Dorcet,*[‡] *Cristelle Mériadec,*[∥] *Soraya Ababou-Girard,*[∥] *Stéphanie Fryars,*[‡] *Gabriel Loget*[‡,*]

‡Univ Rennes, CNRS, ISCR (Institut des Sciences Chimiques de Rennes)-UMR6226 – ScanMAT-UMS2001, F-35000 Rennes, France.

†Department of Materials Science and Engineering, School of Molecular Science and Engineering, Vidyasirimedhi Institute of Science and Technology (VISTEC), Rayong, 21210, Thailand.

§Research Network of NANOTEC-VISTEC on Nanotechnology for Energy, Vidyasirimedhi Institute of Science and Technology (VISTEC), Rayong, 21210, Thailand

∥Univ Rennes, CNRS, IPR (Institut de Physique de Rennes)-UMR 6251, F-35000 Rennes, France

AUTHOR INFORMATION

Corresponding Author

*gabriel.loget@univ-rennes1.fr

ABSTRACT

Metal-insulator-semiconductor (MIS) junctions based on *n*-Si have proven to be effective electrodes in terms of electrocatalysis activity and durability for performing photoelectrochemical water oxidation. Here, we show that the modification of *n*-Si MIS systems with CoFe Prussian blue (CoFePB) and NiRu Prussian blue (NiRuPB) analogs can modify their properties and allow a direct probing of the interfacial energetics through their redox feature. Our investigations demonstrate the importance of the preparation route and attribute the large upward photovoltage variation found in *n*-Si/SiO_x/Ni/NiRuPB to the increasing inhomogeneity of the metal thin film. Finally, the optimal photoanode was tested for oxygen evolution and urea oxidation reactions. Our findings provide important insights on MIS photoanodes for future development in the field of solar fuel production.

KEYWORDS energy conversion, silicon, metal-insulator-semiconductor (MIS), oxygen evolution reaction, Prussian blue analogs

INTRODUCTION

Photoelectrochemical (PEC) water splitting is a promising solution to convert intermittent sunlight into chemical fuels, which can be stored and used on-demand to produce electricity.[1–3] Upon light absorption, a *p*-type semiconductor photocathode generates excited electrons to drive hydrogen evolution reaction (HER), while a *n*-type semiconductor photoanode employs excited holes to drive oxygen evolution reaction (OER). One of the remaining challenges for the development of this technology is related to the photoanode, which needs to perform OER at a high overpotential ($E^0_{O_2/H_2O}$ = 1.23 V vs reversible hydrogen electrode (RHE)) and high reaction rates. Besides improving the photoanode performance by surface engineering strategies, a parallel concept that can be used to increase the yield of PEC cells consists in replacing OER by a less energetic and/or a more valuable reaction, as it is the case for the urea oxidation reaction (UOR), which allows to produce H_2 from urea-contaminated waters.[4–7] To achieve an efficient PEC design, careful consideration of the material aspects is crucial. Because Si can absorb a wide range of the solar spectrum down to the infrared region (bandgap (E_g) of 1.1 eV) and is widely used in microelectronics and photovoltaics industries, it is promising for meeting photoanode's criteria in practical PEC applications.[8] Moreover, Si exhibits a high hole mobility of 390 ±100 $cm^2\ V^{-1}\ s^{-1}$,[9] reducing the probability of charge recombination that would otherwise lead to the loss in performance. However, Si cannot be used as the stand-alone photoanode due to its poor OER activity and notorious instability in aqueous media.[10] Metal-insulator-semiconductor (MIS) junction is therefore a key structure of the modern Si photoanodes to resolve these issues.[11–13] Coating a metal layer, such as Ni, on the Si photoanode passivated with its oxide layer (SiO_x) can enhance OER catalysis and protect Si from the corrosive environment.[14,15] Another important benefit of the metal coating is the creation of a Schottky

barrier at the MIS solid interface, leading to energy band bending in the semiconductor's space charge region that can facilitate hole transfer to oxidize water.[16,17] For *n*-type Si, a high work-function metal is required to induce the large band bending; however, OER-active metals possess relatively low work function for the purpose (e.g. Fe 4.8, Co 5.0, and Ni 5.2 eV).[17,18] Beyond the classical MIS interface, the Schottky junction formation can be improved by various strategies such as introducing surface inhomogeneity[19–24] or adding a material having a higher work function.[16,25] The first strategy is generally introduced by the electrodeposition of metal nanoparticles, which is a bottom-up approach. Recently, our group reported that increased performances could be obtained by the top-down electrodissolution of a metal thin film.[7]

Prussian blue analogs (PBs) have been recognized as one type of coordination polymers constituted of transition-metal cations bridged *via* cyanide ions.[26] CoFe Prussian blue (CoFePB) and NiRu Prussian blue (NiRuPB) analogs can undergo rapid and reversible redox transfer at formal potential ($E^{0'}$) values of approximately 0.45 and 0.90 V vs saturated calomel electrode (SCE), respectively,[27,28] which are typically more positive than the flat-band potential of *n*-Si.[29] If their immobilization at the MIS surface can increase the Schottky barrier at the MIS interface, they could be useful for their electrocatalytic properties as Co, Fe, Ru, and Ni have been considered as excellent active sites for the OER reaction.[30] In particular, CoFePB has been regarded as a promising OER catalyst[31,32] and has been coupled with several photoanodes such as $BiVO_4$,[33–36] α-Fe_2O_3[37], TiO_2,[38], and Si nanowires.[39] Besides, the redox feature in Prussian blue analogs can be utilized to directly probe the interfacial energetics of the photoanode. In our previous work,[7] we reported a simple electrodissolution method that allows in a single step to increase the performance of Si/SiO_x/Ni MIS photoelectrodes and, at the same time, coat the interface with a NiFe Prussian blue analog redox-active probe. We have also shown that such a

method is efficient for elucidating the PEC properties of catalytic MIS photoanodes in mild conditions.[7]

Herein, we report the derivatization of Si/SiO_x/metal (M = Co or Ni) MIS electrodes with two Prussian blue analogs (CoFePB and NiRuPB) by inherently different approaches: spontaneous chemical modification and electrochemical modification, respectively, to prepare Si/SiO_x/Co/CoFePB and Si/SiO_x/Ni/NiRuPB electrodes. We characterize these surfaces and demonstrate that their distinct photovoltage strongly depends on the morphology of the metal layer that is controlled by the preparation method. Finally, we test the best photoanode for OER and UOR photoelectrocatalysis.

METHODS

Reagents

Acetone (MOS electronic grade, Erbatron from Carlo Erba) and anhydrous ethanol (RSE electronic grade, Erbatron from Carlo Erba) were used without further purification. The ultrapure water had a resistivity of 18.2 MΩ cm (Purelab Classic UV). Sulfuric acid (96%, VLSI grade Selectipur) and hydrogen peroxide (30%, VLSI, Sigma-Aldrich) were purchased from BASF and Sigma Aldrich, respectively. KOH (pellets for analysis) was purchased from Merck, KCl (99%) was purchased from Acros. $K_3Fe(CN)_6$, $K_4Ru(CN)_6$, HCl, and urea were purchased from Sigma Aldrich.

Surface preparation

All vials and tweezers used for cleaning of silicon were previously decontaminated in 3/1 v/v concentrated H_2SO_4/30% H_2O_2 at 105 °C for 30 min, followed by copious rinsing with ultrapure

water. *Caution*: the concentrated aqueous H_2SO_4/H_2O_2 (piranha) solution is very dangerous, particularly in contact with organic materials, and should be handled extremely carefully. The *n*-type silicon (0.3–0.7 Ω cm resistivity, phosphorus-doped, single side polished, 275–325 μm) (100) and p^+-type silicon wafers (0.001 Ω cm resistivity, boron-doped, single side polished 275–325 μm) (100) were purchased from Siltronix. All the Si surfaces were degreased by sonication in acetone, ethanol, and ultrapure water for 10 min, respectively. The surfaces were then decontaminated and oxidized in piranha solution at 105 °C for 30 min, followed by rinsing with copious amounts of ultrapure water.

Metal thin film deposition

The Co (thickness = 50 nm) and Ni (thickness = 25 nm) thin films were deposited on the clean Si/SiO_x surfaces by sputtering with a Leica EM ACE600 coating system (target purity: 99.8%, Leica). For Co deposition, the Ar pressure for sputtering was 3.5×10^{-2} mbar, the current was 115 mA and the deposition rate was approximately 0.04 nm s^{-1}. For Ni deposition, the Ar pressure was 2×10^{-2} mbar, the current was 100 mA and the deposition rate was about 0.13 nm s^{-1}. Pre-sputtering time of 1 min was performed for both Co and Ni thin films, the thickness of the film was determined in situ by a quartz crystal microbalance and TEM observation. After deposition, the system was degassed with N_2.

Electrode fabrication

The coated surfaces were further processed to fabricate electrodes. The Ohmic contact was done on the backside of Si wafer by scratching the surface with a diamond glass cutter; then a droplet of InGa eutectic and a metal wire were applied on the scratched part. A thin layer of silver paste (Radiospares) was painted to cover the InGa eutectic contact as well as a part of the metal wire. After drying of the paste, epoxy resin (Loctite 9460, Henkel) was deposited to shield

the backside and frontside of the surface except an active area comprised between 0.1 and 0.25 cm^2, note that the exact geometrical value was precisely measured using the ImageJ software before the (photo)electrochemical experiments. The electrodes were baked in the oven at 90 °C for 1 h to cure the epoxy resin.

Preparation of the Prussian blue analog coatings

The Co-coated electrodes were chemically modified with CoFePB using a freshly-prepared 5 mM $K_3Fe(CN)_6$ solution (pH = 5.5). After dipping for the required time, the electrode was removed from the electrolyte, copiously rinsed with ultrapure water, and dried under an Ar stream. The Ni-coated electrodes were electrochemically modified with NiRuPB using a freshly-prepared 1 mM $K_4Ru(CN)_6$ electrolyte (pH adjusted to 2.5 with concentrated HCl). The electrodes were modified in a two-electrode setup using a SP-150 Bio-Logic potentiostat. The Ni-coated electrode was employed as the anode and a large Pt mesh electrode as the cathode in a beaker filled with the electrolyte. The Pt mesh was placed on the beaker wall and the anode was placed in front of the counter electrode and sequential oxidation pulses of 1 s at 0.67 mA cm^{-2} were imposed followed by resting time of 3 s at 0 mA cm^{-2}. The p^+-Si substrates were modified in the dark and the *n*-Si substrates were modified under illumination through the Pt mesh counter electrode with a 150-W quartz halogen lamp equipped with an optical fiber (OSL2 from Thorlabs). After the desired number of cycles was imposed, the electrode was removed from the cell, copiously rinsed with ultrapure water, and dried under an Ar stream.

Electrochemical and photoelectrochemical experiments

Cyclic voltammetry (CV), chronoamperometry (CA), and open-circuit potential (OCP) measurements were performed in a three-neck cell comprising a quartz window. The reference electrodes were a KCl-saturated calomel electrode (SCE) for the measurements in 1 M KCl and a

Hg/HgO (1 M KOH) electrode for the measurements in alkaline solution. The working electrode was placed in front of the quartz window. The light was provided by a solar simulator (LS0106, LOT Quantum Design) equipped with an AM 1.5 G filter. The power density of the light source was measured before experiments at the position of the photoelectrode using an ILT1400 radiometer (International Light Technologies) to ensure the right power density (100 mW cm^{-2}). Electrochemical measurements were performed with a Zennium potentiostat (Zahner). The potentials versus Hg/HgO (1 M KOH) were converted into potentials versus reversible hydrogen electrode (RHE) using the following relation:

$$E_{RHE} = E_{Hg/HgO} + 0.098 + 0.059pH = E_{Hg/HgO} + 0.924 \quad (1)$$

All reported potentials were intentionally not corrected by the Ohmic drop. Unless specified, the CVs for CoFePB and NiRuPB were recorded at 10 and 25 mV s^{-1}, respectively and CVs for OER and UOR were recorded at 10 mV s^{-1}. Note that the sweep rate of 25 mV s^{-1} was used for preventing the degradation of NiRuPB that was found to occur at lower values.

Solid-state impedance measurements

The front contact of the photoanodes consisted of InGa eutectic, Ag paste and a metal wire and was covered by epoxy resin to increase resistance and and block light penetration. Impedance measurements were performed in a solid-state configuration by employing the back contact and the front contact as a working electrode and a counter/reference electrode, respectively. Space-charge capacitances (C_{sc}) of the semiconductor were extracted by fitting the impedance with an equivalent circuit (as shown in the inset of Figure S14) consisting of a resistor (R_{series}) in a series connection with a parallel resistor (R_{par}) and a parallel capacitor (C_{par}). The parallel capacitor is combination of series contributions that consists of the space-charge capacitance (C_{sc}) and the SiO_x capacitance (C_{ox}).

$$\frac{1}{C_{\mathrm{par}}} = \frac{1}{C_{\mathrm{sc}}} + \frac{1}{C_{\mathrm{ox}}} \quad (2)$$

The C_{ox} was determined by the following relationship:

$$C_{\mathrm{ox}} = \frac{\varepsilon_0 \varepsilon_{\mathrm{SiO_x}}}{t_{\mathrm{SiO_x}}} \quad (3)$$

where is ε_0 the vacuum permittivity (8.85×10^{-14} F cm^{-1}), ε_{SiOx} is the relative permittivity of SiO_x and is assumed to be the same as SiO_2 (3.9). The thickness of SiO_x is estimated (2 nm). Assuming only C_{sc} that varies with the changing potential, the reverse-bias dependence of the inverse square of the space-charge capacitance (C_{sc}^{-2}) is given by the Mott-Schottky relationship:

$$C_{\mathrm{sc}}^{-2} = \frac{2}{\varepsilon_0 \varepsilon_{\mathrm{Si}} q N_{\mathrm{d}}} \left(V - E_{\mathrm{fb}} - \frac{kT}{q} \right) \quad (4)$$

where ε_{Si} is the relative permittivity of Si (11.7), q is the elementary charge (1.6×10^{-19} C), N_d is the donor concentration in the semiconductor, V is the applied voltage, E_{fb} is the flat-band potential, k is the Boltzmann's constant (1.38×10^{-23} m^2 kg s^{-2} K^{-1}) and T is the temperature (298 K). E_{fb} was determined from the value of the x-intercept of the linear region of the Mott-Schottky plot plus kT/q (0.026 V). In order to check the validity of the curves, we have calculated the doping density based on the following relation, obtained by substitution of the Mott-Schottky equation: The slope of *n*-Si/SiO_x/Ni/NiRuPB-150cy (Figure 4f), gives a N_d value of 6.27×10^{16} cm^{-3}, which is in the same range of the resistivity value given by the wafer manufacturer (0.3–0.7 Ω cm). The barrier height (ϕ_b), was then calculated using the following relation:

$$\phi_{\mathrm{b}} = -qE_{\mathrm{fb}} + V_{\mathrm{n}} \quad (5)$$

With V_n being the energy difference between the conduction band and the Fermi level, that was calculated using the following equation:

$$V_{\mathrm{n}} = kT \ln\left(\frac{N_{\mathrm{c}}}{N_{\mathrm{d}}}\right) \quad (6)$$

N_c, the density of states in the conduction band was calculated by:

$$N_c = 2\left(\frac{2\pi m_e^* kT}{h^2}\right)^{3/2} (7)$$

With m_e* being the effective mass of electron in crystalline Si (9.389×10^{-31} kg) and h the Planck constant (6.63×10^{-34} J s). The above equations allowed to calculate a V_n value of 0.15 eV. Thus, using the x-intersect of the linear fit of the Mott-Schottky curves and the slope, the ϕ_b values of 0.75 eV and 0.57 eV were calculated for *n*-Si/SiO_x/Ni/NiRuPB-150cy and *n*-Si/SiO_x/Ni/NiRuPB-0cy, respectively.

Surface characterization

Scanning electron microscopy (SEM) was performed using a JSM 7100 F (JEOL). The sample was prepared for transmission electron microscopy (TEM) analysis as follows. First, the sample was cut in half using a dicing saw fitted with a diamond wire (Precision Diamond Wire Saw, Well 3241, Escil). The two fragments were then glued (G1 epoxy resin with hardener, Gatan) as follows: Si/SiO_x/CoFePB(NiRuPB)/glue/CoFePB(NiRuPB)/SiO_x/Si. This mounting was then cut to fit the TEM-slot (Leica) using a dicing saw. It was then glued onto the slot with the epoxy resin. The slot was then fixed onto a tripod using a mounting adhesive (crystal bond 509, cat#50400–01, Electron Microscopy Sciences) then polished (on both sides) using a sequence of polyamide/diamond papers with a range of particle sizes (from 30 to 1 μm). Finally, a felt polishing pad with colloidal silica was applied, with a final thickness for the area of interest of 20 μm. The slot was further thinned using dimpling grinder (Model 200, Fischione instruments) down to a 10-μm-thick target area before being further processed onto an ion milling machine (low angle ion milling and polishing system, Model 1010, Fischione instruments) to reach a final thickness of <100 nm for TEM analysis. TEM and scanning transmission electron microscopy (STEM) were performed with a JEM 2100 LaB6 (JEOL) equipped with a Silicon Drift Detector

(SDD) - X-Max (Oxford Instruments) and the AZtec software to perform energy-dispersive X-ray spectroscopy and elemental mapping. XPS measurements were performed with an Mg K_{alpha} (hν = 1254.6 eV) X-ray source and an Al source (hν = 1486.6 eV) using a VSW HA100 photoelectron spectrometer with a hemispherical photoelectron analyzer, working at an energy pass of 20 eV for survey and resolved spectra. The experimental resolution was 1.0 eV. Unless specified, C1s set at 284.8 eV was used as the energy reference for all the analyses. Reflectance spectra were acquired on a Shimadzu UV-3600Plus photometer with an integrating sphere (ISR-603) and the data were converted into Kubelka-Munk function.

RESULTS & DISCUSSION

The Si/SiO_x/M/PB preparation methods are illustrated in Figure 1a. First, the planar Si/SiO_x substrates were prepared by chemically oxidizing (p^+- or *n*-) Si (100) wafers to create the SiO_x tunneling layer (~1.9 nm). Following that, a metal thin film (Co, thickness = 50 nm and Ni, thickness = 25 nm) were deposited on the SiO_x surface by DC magnetron sputtering to prepare the Si/SiO_x/M MIS surfaces. For the modification with CoFePB, the Si/SiO_x/Co MIS surfaces were dipped in the $K_3Fe^{III}(CN)_6$ solution (measured pH = 5.5) under gentle stirring. After an immersion time of 1 min, the color of the modified electrode was changed to deep blue (UV-VIS absorption spectra of the unmodified and modified electrodes are shown in Figure S1), implying that CoFePB spontaneously forms on the surface. The modification time was varied between 0 and 30 min and the samples are referred to as 'Si/SiO_x/Co/CoFePB-#m', with #m being the deposition time in minutes. In contrast, for the modification with NiRuPB, Si/SiO_x/Ni MIS surfaces were modified by NiRuPB using an electrodissolution method, similar to that reported

in our previous report,[7] but with an acidic (pH 2.5) $K_4Ru^{II}(CN)_6$ solution. In short, we applied sequential current cycles comprising an anodic pulse (1 s), followed by a resting time (3 s, chronopotentiometry curves are shown in Figure S2). The electrode modification was controlled by the number of cycles between 0 and 200 cycles. The samples were designated as 'Si/SiO_x/Ni/NiRuPB-#cy', with #cy being the number of imposed electrochemical cycles.

The elemental composition of the outermost part of the surfaces was analyzed by X-ray photoelectron spectroscopy (XPS), recorded before and after modification on the p^+-Si/SiO_x/M surfaces (Figure 1b). The XPS survey spectra confirmed the presence of all expected elements for both Co- and Ni-based samples: Co, Fe, C, N, and O for p^+-Si/SiO_x/Co/CoFePB-5m and Ni, Ru, C, N, and O for p^+-Si/SiO_x/Ni/NiRuPB-100cy. The presence of O before and after modification is attributed to the native metal oxide/hydroxide that spontaneously forms on the M surface in ambient conditions. In high-resolution XPS spectra (Figure S3 and S4), p^+-Si/SiO_x/Co/CoFePB-5m electrode exhibited Co $2p_{3/2}$ and Co $2p_{1/2}$ peaks at 781.8 and 797.6 eV, which is in good agreement with the literature.[40] In the Fe 2p region, the main peak at 708.4 eV corresponds to Fe $2p_{3/2}$ for Fe^{II}.[41] For p^+-Si/SiO_x/Ni/NiRuPB-100cy, the Ru $3d_{5/2}$ and Ru $3d_{3/2}$ peaks were found at 280.6 eV and 286.8 eV, respectively, which is consistent with the literature.[42] It is also interesting to note that K^+ incorporation, which is known to occasionally occur in PBs,[40] was only observed for p^+-Si/SiO_x/Co/CoFePB-5m. In both cases, the PB derivatization was evidenced by a drastic increase of the XPS C 1s and N 1s peaks after the modification. The presence of the CN bridges in p^+-Si/SiO_x/Co/CoFePB and p^+-Si/SiO_x/Ni/NiRuPB electrodes was also evidenced by Raman spectroscopy, recorded in dry air. In Figure S5, Raman peaks were detected in a range of 2000 - 2200 cm^{-1}, which is consistent with the stretching vibrations of the triple CN bond in PBs.[43]

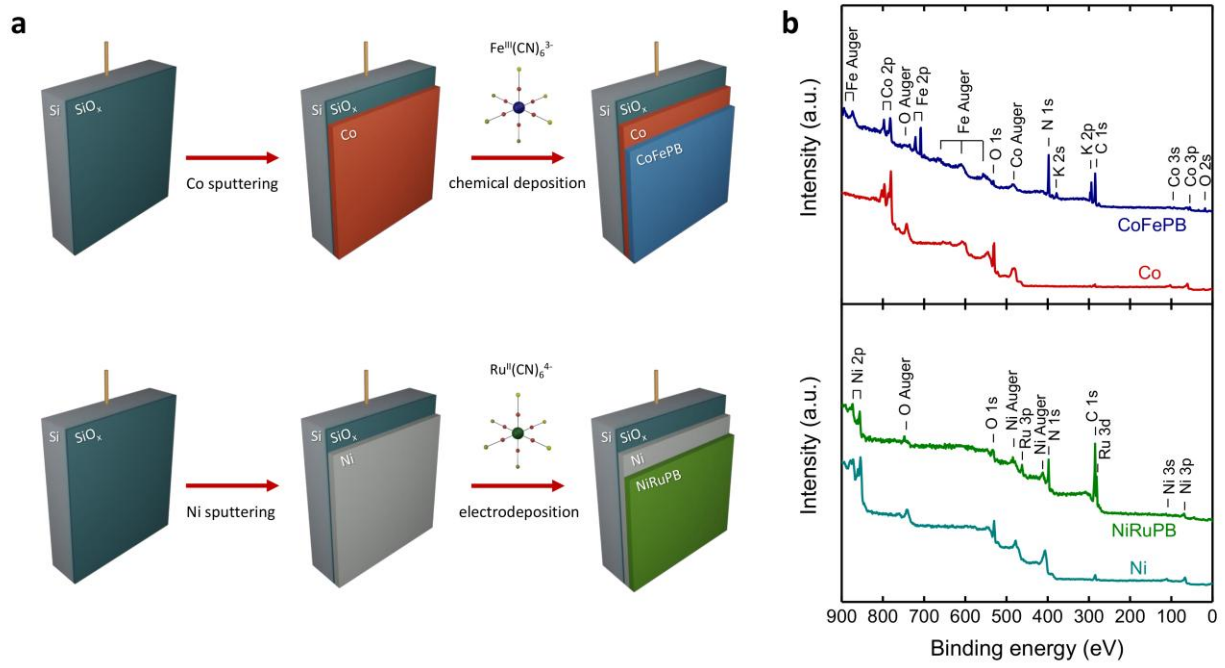

Figure 1. (a) Schematics of Si/SiO_x/Co/CoFePB prepared by sputtering and chemical deposition processes (top panel) and Si/SiO_x/Ni/NiRuPB prepared by sputtering and electrodeposition processes (bottom panel). (b) XPS survey spectra recorded for (red) unmodified p^+-Si/SiO_x/Co/CoFePB-0m and (blue) p^+-Si/SiO_x/Co/CoFePB-5m (top panel) and (turquoise) p^+-Si/SiO_x/Ni/NiRuPB-0cy and (green) p^+-Si/SiO_x/Ni/NiRuPB-100cy (bottom panel).

The electrochemical activity of the non-photoactive p^+-Si/SiO_x/M MIS anodes at different modification stages was recorded by cyclic voltammetry (CV) in 1 M KCl in the dark. Figure 2a shows that, in contrast to the unmodified p^+-Si/SiO_x/Co/CoFePB-0m surface, all CVs recorded on modified p^+-Si/SiO_x/Co/CoFePB revealed a marked redox activity at $E^{0'}$ ~0.5 V vs SCE. According to the literature, this wave comprises two convoluted redox waves corresponding to the Fe^{III}/Fe^{II} and the Co^{III}/Co^{II} couples.[28] Meanwhile, a similar behavior was observed on p^+-Si/SiO_x/Ni/NiRuPB, that is, no redox wave was present at 0cy and a reversible wave appeared at $E^{0'}$ ~0.96 V vs SCE (Figure 2b) for all modified electrodes, a value which is close to that reported for the Ru^{III}/Ru^{II} system in NiRuPB.[27] The small peak to peak difference as well as the

linear relationship between the current density and the scan rate (Figure S6) is well in line with a reversible redox immobilized system.[44] Besides, the peak intensity as a function of the modification time or cycle is informative about the amount of deposited redox-active centers. In the case of p^+-Si/SiO_x/Co/CoFePB, an increasing time leads to an increase of the immobilized CoFePB while, for p^+-Si/SiO_x/Ni/NiRuPB, an increase in modification cycle is not correlated with an increase of the surface NiRuPB. According to Figure 2b, the number of NiRuPB redox-active centers remains similar from 50cy to 150cy and decreases at 200cy, suggesting a more complex modification mechanism than that of CoFePB. Figure 2c compares the signal obtained for p^+-Si/SiO_x/Ni/NiRuPB-150cy and p^+-Si/SiO_x/Co/CoFePB-30m and shows clearly the $E^{0'}$ difference of 0.44 V recorded for the two PB systems.

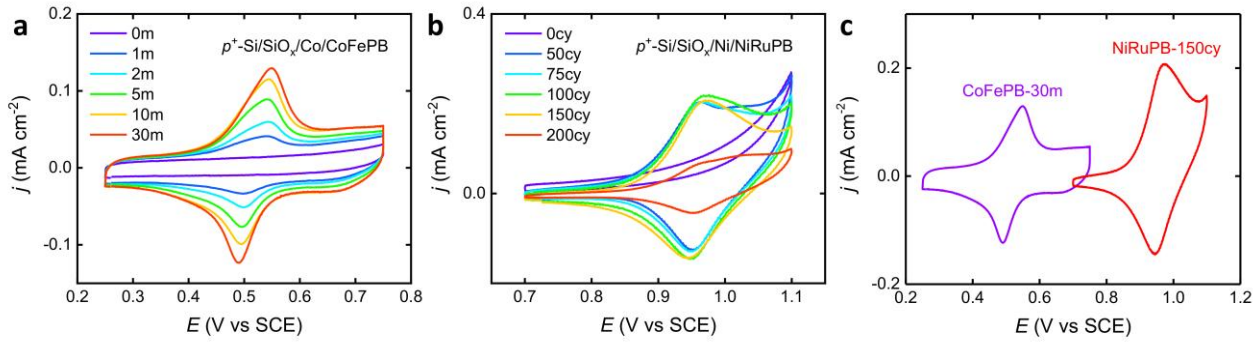

Figure 2. Cyclic voltammetry of (a) p^+-Si/SiO_x/Co/CoFePB with different chemical deposition times (from 0 to 30 min) and (b) p^+-Si/SiO_x/Ni/NiRuPB electrodes with different number of cycles (from 0 to 200 cycles). (c) Comparison of the position of the reversible redox waves recorded with p^+-Si/SiO_x/Co/CoFePB-30m and p^+-Si/SiO_x/Ni/NiRuPB-150cy. All measurements were performed in 1 M KCl, the CVs of CoFePB- and NiRuPB-derivatized electrodes were recorded at 10 and 25 mV s^{-1}, respectively.

The photoelectrochemistry of the derivatized photoactive *n*-Si/SiO_x/M/PB MIS photoanodes is now discussed. In Figure 3a and d, the redox waves measured on photoactive *n*-Si-based electrodes under illumination with simulated sunlight (red CVs) are compared with the ones recorded in the dark on non-photoactive p^+-Si-based electrodes (black CVs). From these curves,

it can be seen that the PB redox waves appeared at a lower $E^{0'}$ value on illuminated *n*-Si compared to that obtained on the p^+-Si electrodes, evidencing the photovoltage generation. CVs under illumination were recorded for all modification time and cycle (Figure S7) and several are plotted in Figure 3b and e, for *n*-Si/SiO_x/Co/CoFePB and *n*-Si/SiO_x/Ni/NiRuPB, respectively. A considerable difference appears in these curves. Figure 3b and S7a show that that the $E^{0'}$ position remained relatively unchanged for all *n*-Si/SiO_x/Co/CoFePB electrodes. Conversely, the $E^{0'}$ value of *n*-Si/SiO_x/Ni/NiRuPB decreased with an increasing cycle number as illustrated in Figure 3e and S7b. To verify the changes in the photovoltage with the modification steps, two different methods to determine the photovoltage values were conducted separately: (1) from dark and light open-circuit potential (OCP) measurements on the *n*-Si/SiO_x/M/PB photoanodes (Figure S8a,b) and (2) the difference of $E^{0'}$ values extracted from the CV of p^+-Si/SiO_x/M/PB in the dark and the *n*-Si/SiO_x/M/PB CV under illumination. The resulting photovoltage values were plotted as a function of modification time and cycle number in Figure 3c and f for *n*-Si/SiO_x/Co/CoFePB and *n*-Si/SiO_x/Ni/NiRuPB, respectively. The photovoltage values determined for *n*-Si/SiO_x/Co/CoFePB were relatively similar to both methods and the photovoltage did not change considerably as a function of the modification time, with an average value of 0.25 ±0.02 V.

The measurements on *n*-Si/SiO_x/Ni/NiRuPB yielded different results. First, one can observe that the two measurement methods gave photovoltage values with a variation that increased with the cycle number. Although this is still not fully understood, we do think that this is related to the morphology change of the Ni/NiRuPB layer (*vide infra*). Indeed, it has been reported that OCP measurements are not always a suitable method for determining the photovoltage for semiconductor/catalyst systems, especially when the catalysts are electrolyte-permeable.[45]

However, both methods yielded a similar trend, with a photovoltage enhancement with an increasing modification time ranging from 0 to 150 cycles (Figure 3f), followed by a photovoltage decrease at 200 cycles. The optimum was reached for *n*-Si/SiO_x/Ni/NiRuPB-150cy, which exhibited the highest photovoltage (0.37 V and 0.46 V as determined by OCP and $E^{0'}$ measurements, respectively).

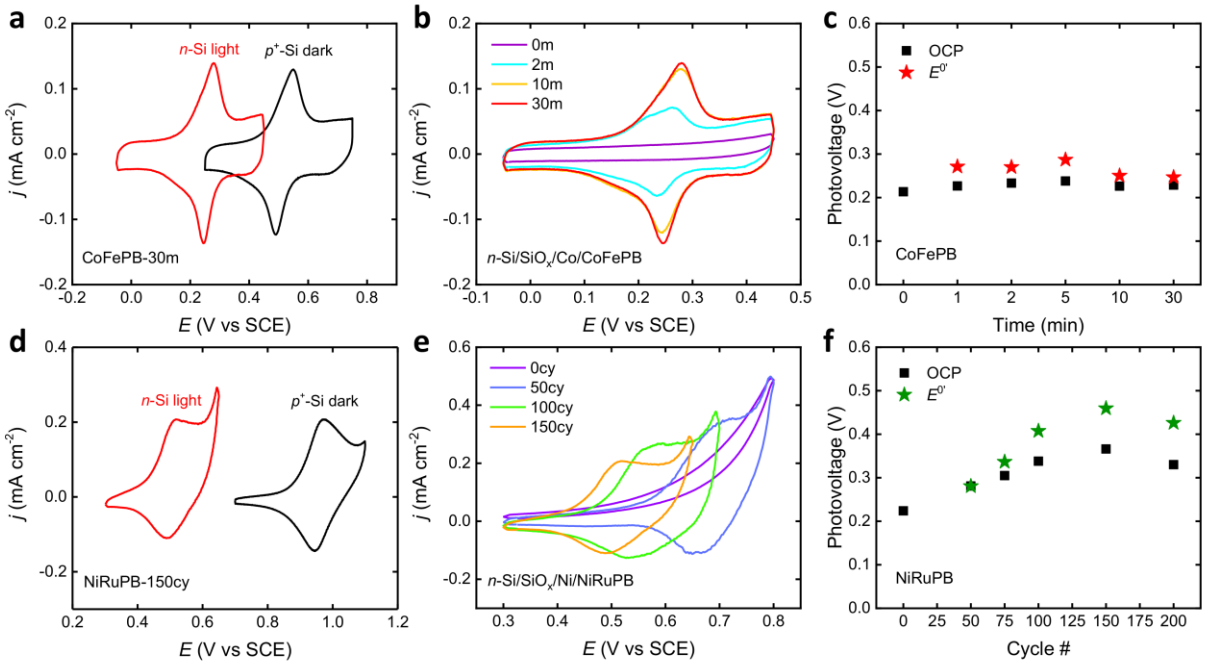

Figure 3. (a) CVs recorded in the dark on (black) p^+-Si/SiO_x/Co/CoFePB-30m and under simulated sunlight on (red) *n*-Si/SiO_x/Co/CoFePB-30m. (b) CVs recorded under simulated sunlight on *n*-Si/SiO_x/Co/CoFePB with modification times of 0, 2, 10, and, 30 minutes. (c) Photovoltages determined by OCP (black squares) and $E^{0'}$ (red stars) measurements on Si/SiO_x/Co/CoFePB as a function of the deposition time. (d) CVs recorded in the dark on (black) p^+-Si/SiO_x/Ni/NiRuPB-150cy and under simulated sunlight on (red) *n*-Si/SiO_x/Ni/NiRuPB-150cy. (e) CVs recorded under simulated sunlight on *n*-Si/SiO_x/Ni/NiRuPB with 0, 50, 100, and 150 cycles. (f) Photovoltages determined by (black squares) OCP and (green stars) $E^{0'}$ measurements on Si/SiO_x/Ni/NiRuPB as a function of the number of cycles. All measurements were measured in 1 M KCl. CVs of Si/SiO_x/Co/CoFePB and Si/SiO_x/Ni/NiRuPB electrodes were recorded at 10 and 25 mV s^{-1}, respectively.

To understand these results and, particularly, the striking difference in the photovoltage evolution, we performed morphological characterizations of the modified surfaces. For that, p^+-

Si/SiO_x/Co/CoFePB-5m and p^+-Si/SiO_x/Ni/NiRuPB-150cy were observed by scanning electron microscopy (SEM) and atomic force microscopy (AFM). While no considerable change was observed on top-view SEM images for the p^+-Si/SiO_x/Co/CoFePB surface before and after modification, (Figure S9a,b), the porosity of the p^+-Si/SiO_x/Ni/NiRuPB surface seemed to considerably increase after the treatment (Figure S9c,d). This observation was confirmed by AFM inspection (Figure 4a,d, and Figure S10) which revealed that the Co/CoFePB-5m coating consisted of densely packed nanosized grains with low roughness (root-mean-square (RMS) roughness = 1.24 nm) while Ni/NiRuPB-150cy contained many randomly-dispersed and non-uniform islands and exhibited a much higher roughness (RMS roughness = 12.16 nm). The cross-sectional view of both derivatized MIS interfaces was observed by transmission electron microscopy (TEM), as shown by Figure 4b for p^+-Si/SiO_x/Co/CoFePB-5m and Figure 4e for p^+-Si/SiO_x/Ni/NiRuPB-150cy. The analysis of both surfaces showed that the SiO_x layer had a thickness in the order of 2 nm (Figure S11 and 4e). Figure 4b shows that a low density grey-colored thin layer with a thickness of ~15 nm was deposited on the top of the Co thin film. Elemental analysis by energy-dispersive X-ray spectroscopy (EDS) revealed that layer to be the CoFePB coating (Figure S12). While the Co/CoFePB-5m film was observed to be homogeneous on Si/SiO_x, TEM measurements revealed the high inhomogeneity of the p^+-Si/SiO_x/Ni/NiRuPB-150cy surface. Indeed, Figure 4e and Figure S13 show that dispersed nanosized Ni islands are in contact with the SiO_x surface on the p^+-Si/SiO_x/Ni/NiRuPB-150cy surface, in good agreement with what was previously observed by SEM (Figure S9d) and AFM (Figure 4d). In this case, although Ni was imaged by TEM, the NiRuPB layer could not be clearly observed (EDS investigation revealed that NiRuPB diffused inside the resin that was used for shielding the sample for TEM preparation). To summarize, SEM, AFM, and TEM analyses showed that the

Si/SiO_x/Co/CoFePB-5m and the Si/SiO_x/Ni/NiRuPB-150cy surfaces exhibited homogeneous and inhomogeneous Si/SiO_x/M MIS junctions, respectively. The photovoltage trends that were previously observed can be rationalized by these distinct morphologies. Specifically, the chemical modification with CoFePB preserves the integrity of the homogenous *n*-Si/SiO_x/Co Schottky contact and the CoFePB thin film only coats the outermost part of the Co (Figure 4c) and does not affect the thermodynamics of the MIS junction. In contrast, during electrochemical modification of *n*-Si/SiO_x/Ni with NiRuPB, the initially conformal metal film is partially dissolved leading to a porosification of the Ni thin film, which makes the *n*-Si/SiO_x/Ni MIS junction highly inhomogeneous as shown in Figure 4f. This relationship between inhomogeneity and photovoltage is in good agreement with what has been recently reported in the literature.[7] Indeed, several photoanodes based on *n*-Si Schottky junctions, prepared by electrodeposition or electrodissolution, exhibit an improvement of performance with increased inhomogeneity.[7,22,23] This phenomenon can be explained by the replacement of the low barrier *n*-Si/SiO_x/M junction by another junction having a higher barrier height (Si/SiO_x[46] or Si/SiO_x/MO_xH_y[23]),[47] leading to an overall improvement of the photovoltage.[15,23] Note that, in the present case, Si/SiO_x/PB could also be generated and potentially affect the overall barrier height (this is, however, unlikely as we will discuss later).

In order to understand how the morphology evolution of the *n*-Si/SiO_x/M MIS junction affects the energetics of the surface, we performed solid-state measurements (see the method section for more details) on *n*-Si/SiO_x/Ni/NiRuPB-0cy and *n*-Si/SiO_x/Ni/NiRuPB-150cy, as NiRuPB modification leads to the highest photovoltages. As shown in Figure 4g, current-voltage curves of *n*-Si/SiO_x/Ni/NiRuPB-0cy and *n*-Si/SiO_x/Ni/NiRuPB-150cy solid-state cells show the expected rectifying behavior of a diode. When a positive voltage ($V > 0$) is applied on the

semiconductor side, the valence band edge bends upward near the surface and the majority carriers (electrons) are depleted.[48] Impedance measurements were recorded in this regime to obtain space-charge capacitance values (C_{sc}) that were fitted with an equivalent circuit described in the method section (experimentally determined and fitted Nyquist plots are shown in Figure S14). The effective barrier height can be obtained from Mott-Schottky analysis, which was done on our solid-state devices as reported in a previous report.[17] The results of Figure 4h allowed us to determine the flat-band potential (E_{fb}), the doping density (N_d), and the effective barrier height (ϕ_b) which were calculated to be -0.60 V, 6.27 $\times 10^{16}$ cm^{-3}, and 0.75 eV, respectively for *n*-Si/SiO_x/Ni/NiRuPB-150cy. This value of ϕ_b is relatively in good agreement with previous reports for MIS photoanodes[7,19] and is noticeably higher than the 0.57 eV found for the unmodified and homogeneous *n*-Si/SiO_x/Ni/NiRuPB-0cy. To sum-up, our solid-state impedance results show that the transformation of the Ni thin film which occurs during the derivatization with NiRuPB induces a negative shift of the flat band potential which increases the barrier height of the MIS Schottky junction. This confirms our previous observations and explains why the photovoltage of *n*-Si/SiO_x/Ni/NiRuPB-150cy is significantly higher (Figure 3f). To determine how NiRuPB influences the junction thermodynamics, we performed dark/light OCP measurements on the *n*-Si/SiO_x/Ni/NiRuPB-150cy photoanode before and after NiRuPB was selectively removed by soaking it into a KOH solution for 15 minutes.[27] The photovoltages derived from these OCP measurements were statistically identical (Figure S15), showing that the photovoltage improvement is independent of NiRuPB but related to the nature of the *n*-Si/SiO_x/M.

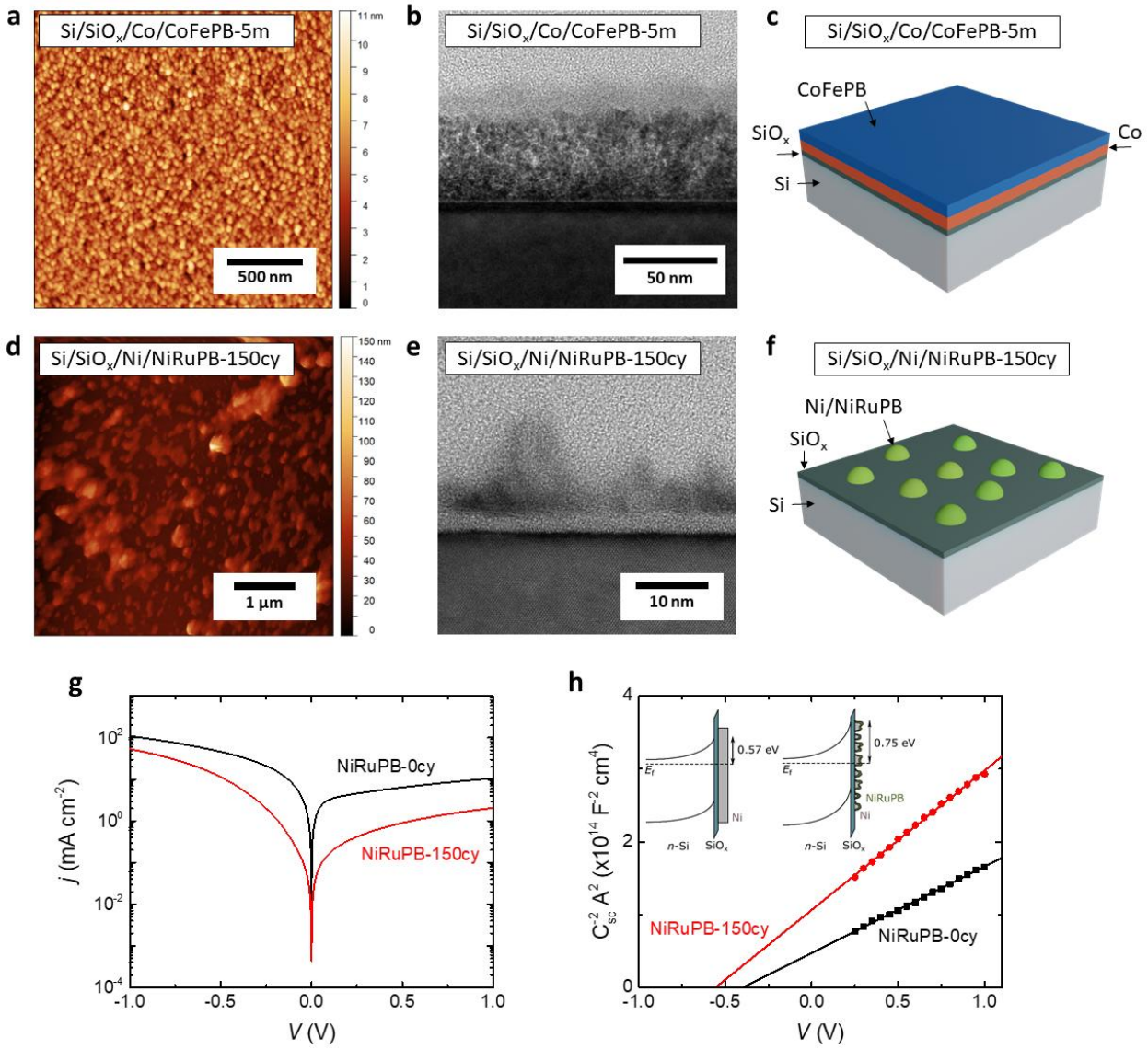

Figure 4. (a, d) Top-view AFM images, (b, e) cross-sectional TEM images and (c, f) schematics surface structures of (top panel) p^+-Si/SiO_x/Co/CoFePB-5m and (bottom panel) p^+-Si/SiO_x/Ni/NiRuPB-150cy. (g) Current-voltage curves and (h) Mott-Schottky plots of (black) *n*-Si/SiO_x/Ni/NiRuPB-0cy and (red) *n*-Si/SiO_x/Ni/NiRuPB-150cy; inset shows the band energy diagrams.

Finally, we decided to test the best photoanode (*n*-Si/SiO_x/Ni/NiRuPB-150cy) for photoelectrocatalysis. For that, we compared its activity and that of its non-photoactive counterpart (p^+-Si/SiO_x/Ni/NiRuPB-150cy) in a highly alkaline medium (1 M KOH) for OER and also for UOR because Ni-based compounds have been considered as prominent active sites

for both reactions.[4–7] As observed from the typical characteristics of the CVs (Figure 5a), the non-photoactive surface operated in the dark triggered both reactions whereas *n*-Si/SiO_x/Ni/NiRuPB-150cy did so only under illumination. The latter showed high photocurrent density values of 8.3 and 17.5 mA cm^{-2} at 1.23 V vs RHE for OER and UOR, respectively, under simulated sunlight. The non-constant photocurrent in the saturated regime (blue CV of Figure 5a) was highly reproducible, several examples of such a non-conventional behavior on MIS photoanodes have been reported in the literature and might involve the SiO_x layer.[46,49] The onset potential, which was defined as the required potential to produce a photocurrent density of 1 mA cm^{-2}, was measured to be 1.1 and 0.9 V vs RHE for OER and UOR, respectively. The photovoltage can also be estimated from the difference of onset potential obtained for p^+-Si-based electrode in the dark and the *n*-Si-based electrode under illumination and was found to be 0.43 and 0.41 V for OER and UOR, respectively, which is in good agreement with previously measured in 1 M KCl for this photoanode using the $E^{0'}$ method (Figure 3f, Figure S16b). In Figure 5b, the stability of the photoanodes during OER and UOR was evaluated by chronoamperometry (CA) at +1.23 V vs RHE under simulated sunlight. As reported, within 1 h, the photocurrent density of the photoanode maintained during OER, in contrast to UOR, for which the current density rapidly dropped to ~30% of the initial current density. This suggests that the photoanode is very stable for OER but not for performing UOR for a prolonged time, possibly caused by surface pollution, which is often encountered in UOR at Ni-based electrocatalysts.[7,50] After electrolysis, CVs of the photoanodes were recorded in 1 M KCl to reveal the NiRuPB stability after operations, Figure S17 indicates that the redox wave of the NiRuPB disappeared, implying that NiRuPB did not remain on the electrode surface after operations. This is not surprising given the fact that PBs are not stable at such pH values.[51–53]

However, the stable OER photocurrent density recorded during the potentiostatic measurement (Figure 5b) confirms that the photoanode maintained its stability, and thus that NiRuPB is not acting as a catalyst in our case, in good agreement with our previous report.[7] In contrast, electrolyte-exposed NiOOH sites present on the Ni film[54] are likely responsible for the respective OER[55] and UOR[56] electrocatalysis.

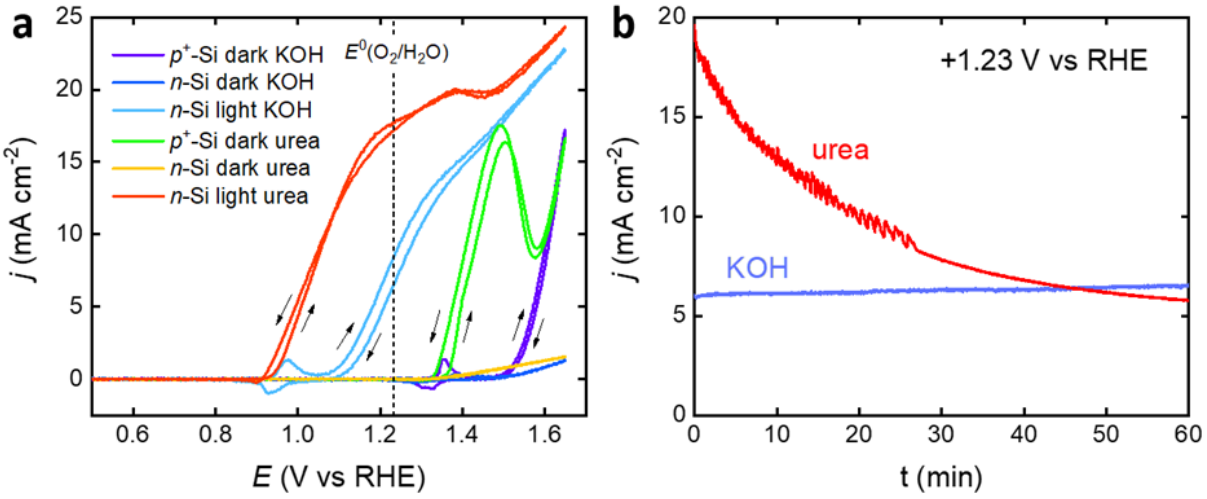

Figure 5. (a) CVs showing the OER and UOR electrocatalysis on p^+-Si/SiO_x/Ni/NiRuPB-150cy and n-Si/SiO_x/Ni/NiRuPB-150cy in 1 M KOH and 0.33 M urea + 1 M KOH (b) CA curves recorded for OER and UOR at +1.23 V vs RHE.

CONCLUSION

In conclusion, we have reported on the structure-property relationships of redox-derivatized MIS anodes. We have shown that CoFePB and NiRuPB can be deposited on MIS electrodes and that these redox species allow to reliably probe the interfacial energetics of the photoanodes. Our studies revealed the importance of the preparation method and ascribed a considerably upward photovoltage variation, found in NiRuPB-derivatized photoanodes, to an increased Schottky junction inhomogeneity occurring through the partial dissolution of the Ni metal thin film. In the

frame of recent results of the literature, this phenomenon can be explained by the conversion of the low barrier *n*-Si/SiO_x/M junction by another junction having a higher barrier height such as Si/SiO_x[45] or Si/SiO_x/MO_xH_y.[23,47] Conversely, this phenomenon was not observed for the chemically-derivatized CoFePB photoanodes which preserved the homogeneity of the Co thin film. Finally, the optimal inhomogeneous *n*-Si/SiO_x/Ni/NiRuPB photoanode exhibited a marked photocurrent density of 8.3 mA cm^{-2} at 1.23 V vs RHE for sunlight-assisted OER with a stable photoresponse. As a short term perspective, we do think that the effect of the metal film thickness is an important parameter that should be studied. Our findings give new insights on MIS photoanodes which should open new pathways for improving MIS photoanodes through structuring strategies, which will be useful for solar fuel generation.

ASSOCIATED CONTENT

Supporting Information

The Supporting Information is available free of charge from https://pubs.acs.org.

Additional surface and PEC characterizations; UV-Vis absorption spectra; high-resolution XPS spectra; Raman spectra; cyclic voltammetry; OCP measurement; SEM images; TEM images; EDS spectra; and solid-state Nyquist plots.

AUTHOR INFORMATION

Corresponding Author

*Gabriel Loget, e-mail: gabriel.loget@univ-rennes1.fr

ORCID

Ponart Aroonratsameruang: 0000-0002-3519-0444

Pichaya Pattanasattayavong: 0000-0001-6374-1840

Vincent Dorcet: 0000-0003-2141-2496

Gabriel Loget: 0000-0003-4809-5013

Notes

The authors declare no competing financial interests.

ACKNOWLEDGMENT

P.A. and P.P. would like to thank the financial support from Vidyasirimedhi Institute of Science and Technology (VISTEC). P.P. acknowledges research grant TRG6280013 jointly funded by Thailand's Synchrotron Light Research Institute (SLRI) and Thailand Research Fund (TRF). G. Taupier and A. Moréac (ScanMAT, SIR) are acknowledged for their help with the Raman measurements. J.-F. Bergamini is acknowledged for his help with AFM experiments.

REFERENCES

(1) Elliott, D. A Balancing Act for Renewables. *Nat. Energy* **2016**, *1*, 15003.

(2) Pinaud, B. A.; Benck, J. D.; Seitz, L. C.; Forman, A. J.; Chen, Z.; Deutsch, T. G.; James, B. D.; Baum, K. N.; Baum, G. N.; Ardo, S.; et al. Technical and Economic Feasibility of Centralized Facilities for Solar Hydrogen Production via Photocatalysis and Photoelectrochemistry. *Energy Environ. Sci.* **2013**, *6*, 1983–2002.

(3) Dumortier, M.; Tembhurne, S.; Haussener, S. Holistic Design Guidelines for Solar

Hydrogen Production by Photo-Electrochemical Routes. *Energy Environ. Sci.* **2015**, *8*, 3614–3628.

(4) Zhu, B.; Liang, Z.; Zou, R. Designing Advanced Catalysts for Energy Conversion Based on Urea Oxidation Reaction. *Small* **2020**, *16*, 1906133.

(5) Boggs, B. K.; King, R. L.; Botte, G. G. Urea Electrolysis: Direct Hydrogen Production from Urine. *Chem. Commun.* **2009**, *32*, 4859.

(6) Wang, G.; Ling, Y.; Lu, X.; Wang, H.; Qian, F.; Tong, Y.; Li, Y. Solar Driven Hydrogen Releasing from Urea and Human Urine. *Energy Environ. Sci.* **2012**, *5*, 8215–8219.

(7) Loget, G.; Mériadec, C.; Dorcet, V.; Fabre, B.; Vacher, A.; Fryars, S.; Ababou-Girard, S. Tailoring the Photoelectrochemistry of Catalytic Metal-Insulator-Semiconductor (MIS) Photoanodes by a Dissolution Method. *Nat. Commun.* **2019**, *10*, 3522.

(8) Luo, Z.; Wang, T.; Gong, J. Single-Crystal Silicon-Based Electrodes for Unbiased Solar Water Splitting: Current Status and Prospects. *Chem. Soc. Rev.* **2019**, *48*, 2158–2181.

(9) Cushing, S. K.; Porter, I. J.; de Roulet, B. R.; Lee, A.; Marsh, B. M.; Szoke, S.; Vaida, M. E.; Leone, S. R. Layer-Resolved Ultrafast Extreme Ultraviolet Measurement of Hole Transport in a Ni-TiO_2-Si Photoanode. *Sci. Adv.* **2020**, *6*, eaay6650.

(10) *Electrochemistry of Silicon and Its Oxide*; Zhang, X. G., Kluwer Academic Publishers: Boston, 2001.

(11) Liu, B.; Feng, S.; Yang, L.; Li, C.; Luo, Z.; Wang, T.; Gong, J. Bifacial Passivation of n -Silicon Metal–Insulator–Semiconductor Photoelectrodes for Efficient Oxygen and Hydrogen Evolution Reactions. *Energy Environ. Sci.* **2020**, *13*, 221–228.

(12) Hemmerling, J.; Quinn, J.; Linic, S. Quantifying Losses and Assessing the Photovoltage Limits in Metal–Insulator–Semiconductor Water Splitting Systems. *Adv. Energy Mater.* **2020**, *10*, *1903354*.

(13) Hendricks, O. L.; Tang-Kong, R.; Babadi, A. S.; McIntyre, P. C.; Chidsey, C. E. D. Atomic Layer Deposited TiO_2–IrO_x Alloys Enable Corrosion Resistant Water Oxidation on Silicon at High Photovoltage. *Chem. Mater.* **2019**, *31*, 90–100.

(14) Lee, S. A.; Choi, S.; Kim, C.; Yang, J. W.; Kim, S. Y.; Jang, H. W. Si-Based Water Oxidation Photoanodes Conjugated with Earth-Abundant Transition Metal-Based Catalysts. *ACS Mater. Lett.* **2020**, *2*, 107–126.

(15) Loget, G. Water Oxidation with Inhomogeneous Metal-Silicon Interfaces. *Curr. Opin. Colloid Interface Sci.* **2019**, *39*, 40–50.

(16) Digdaya, I. A.; Adhyaksa, G. W. P.; Trześniewski, B. J.; Garnett, E. C.; Smith, W. A. Interfacial Engineering of Metal-Insulator-Semiconductor Junctions for Efficient and Stable Photoelectrochemical Water Oxidation. *Nat. Commun.* **2017**, *8*, 15968.

(17) Digdaya, I. A.; Trześniewski, B. J.; Adhyaksa, G. W. P.; Garnett, E. C.; Smith, W. A. General Considerations for Improving Photovoltage in Metal-Insulator-Semiconductor Photoanodes. *J. Phys. Chem. C* **2018**, *122*, 5462–5471.

(18) Ueda, K.; Shimizu, R. Photoelectric Work Function Study on Iron (100) Surface Combined with Auger Electron Spectroscopy. *Jpn. J. Appl. Phys.* **1973**, *12*, 1869–1873.

(19) Hill, J. C.; Landers, A. T.; Switzer, J. A. An Electrodeposited Inhomogeneous Metal-Insulator-Semiconductor Junction for Efficient Photoelectrochemical Water Oxidation.

Nat. Mater. **2015**, *14*, 1150–1155.

(20) Loget, G.; Fabre, B.; Fryars, S.; Mériadec, C.; Ababou-Girard, S. Dispersed Ni Nanoparticles Stabilize Silicon Photoanodes for Efficient and Inexpensive Sunlight-Assisted Water Oxidation. *ACS Energy Lett.* **2017**, *2*, 569–573.

(21) Oh, K.; Mériadec, C.; Lassalle-Kaiser, B.; Dorcet, V.; Fabre, B.; Ababou-Girard, S.; Joanny, L.; Gouttefangeas, F.; Loget, G. Elucidating the Performance and Unexpected Stability of Partially Coated Water-Splitting Silicon Photoanodes. *Energy Environ. Sci.* **2018**, *11*, 2590–2599.

(22) Oh, K.; Dorcet, V.; Fabre, B.; Loget, G. Dissociating Water at N- Si Photoanodes Partially Covered with Fe Catalysts. *Adv. Energy Mater.* **2020**, *10*, 1902963.

(23) Laskowski, F. A. L.; Oener, S. Z.; Nellist, M. R.; Gordon, A. M.; Bain, D. C.; Fehrs, J. L.; Boettcher, S. W. Nanoscale Semiconductor/Catalyst Interfaces in Photoelectrochemistry. *Nat. Mater.* **2020**, *19*, 69–76.

(24) Lee, S. A.; Lee, T. H.; Kim, C.; Choi, M. J.; Park, H.; Choi, S.; Lee, J.; Oh, J.; Kim, S. Y.; Jang, H. W. Amorphous Cobalt Oxide Nanowalls as Catalyst and Protection Layers on N-Type Silicon for Efficient Photoelectrochemical Water Oxidation. *ACS Catal.* **2020**, *10*, 420–429.

(25) Hendricks, O. L.; Scheuermann, A. G.; Schmidt, M.; Hurley, P. K.; McIntyre, P. C.; Chidsey, C. E. D. Isolating the Photovoltaic Junction: Atomic Layer Deposited TiO_2 – RuO_2 Alloy Schottky Contacts for Silicon Photoanodes. *ACS Appl. Mater. Interfaces* **2016**, *8*, 23763–23773.

(26) Zhao, D.; Lu, Y.; Ma, D. Effects of Structure and Constituent of Prussian Blue Analogs on Their Application in Oxygen Evolution Reaction. *Molecules* **2020**, *25*, 2304.

(27) Sinha, S.; Humphrey, B. D.; Bocarsly, A. B. Reaction of Nickel Electrode Surfaces with Anionic Metal-Cyanide Complexes: Formation of Precipitated Surfaces. *Inorg. Chem.* **1984**, *23*, 203–212.

(28) Lezna, R. O.; Romagnoli, R.; De Tacconi, N. R.; Rajeshwar, K. Cobalt Hexacyanoferrate: Compound Stoichiometry, Infrared Spectroelectrochemistry, and Photoinduced Electron Transfer. *J. Phys. Chem. B* **2002**, *106*, 3612–3621.

(29) Röppischer, H. Flatband Potential Studies at the N-Si/Electrolyte Interface by Electroreflectance and C-V Measurements. *J. Electrochem. Soc.* **1995**, *142*, 650.

(30) C. L. McCrory, C.; Jung, S.; M. Ferrer, I.; M. Chatman, S.; C. Peters, J.; F. Jaramillo, T. Benchmarking Hydrogen Evolving Reaction and Oxygen Evolving Reaction Electrocatalysts for Solar Water Splitting Devices. *J. Am. Chem. Soc.* **2015**, *137*, 4347–4357.

(31) Pintado, S.; Goberna-Ferrón, S.; Escudero-Adán, E. C.; Galán-Mascarós, J. R. Fast and Persistent Electrocatalytic Water Oxidation by Co-Fe Prussian Blue Coordination Polymers. *J. Am. Chem. Soc.* **2013**, *135*, 13270–13273.

(32) Han, L.; Tang, P.; Reyes-Carmona, Á.; Rodríguez-García, B.; Torréns, M.; Morante, J. R.; Arbiol, J.; Galan-Mascaros, J. R. Enhanced Activity and Acid pH Stability of Prussian Blue-Type Oxygen Evolution Electrocatalysts Processed by Chemical Etching. *J. Am. Chem. Soc.* **2016**, *138*, 16037–16045.

(33) Ghobadi, T. G. U.; Ghobadi, A.; Soydan, M. C.; Vishlaghi, M. B.; Kaya, S.; Karadas, F.; Ozbay, E. Strong Light–Matter Interactions in Au Plasmonic Nanoantennas Coupled with Prussian Blue Catalyst on $BiVO_4$ for Photoelectrochemical Water Splitting. *ChemSusChem* **2020**, *13*, 2577–2588.

(34) Trzciński, K.; Szkoda, M.; Sawczak, M.; Lisowska-Oleksiak, A. Enhanced Photoelectrocatalytical Performance of Inorganic-Inorganic Hybrid Consisting $BiVO_4$, V_2O_5, and Cobalt Hexacyanocobaltate as a Perspective Photoanode for Water Splitting. *Electrocatalysis* **2020**, 11, 180–187.

(35) Moss, B.; Hegner, F. S.; Corby, S.; Selim, S.; Francàs, L.; López, N.; Giménez, S.; Galán-Mascarós, J. R.; Durrant, J. R. Unraveling Charge Transfer in CoFe Prussian Blue Modified $BiVO_4$ Photoanodes. *ACS Energy Lett.* **2019**, *4*, 337–342.

(36) Hegner, F. S.; Herraiz-Cardona, I.; Cardenas-Morcoso, D.; López, N.; Galán-Mascarós, J. R.; Gimenez, S. Cobalt Hexacyanoferrate on $BiVO_4$ Photoanodes for Robust Water Splitting. *ACS Appl. Mater. Interfaces* **2017**, *9*, 37671–37681.

(37) Shu, J.; Tang, D. Recent Advances in Photoelectrochemical Sensing: From Engineered Photoactive Materials to Sensing Devices and Detection Modes. *Anal. Chem.* **2020**, *32*, 363-377.

(38) Ulusoy Ghobadi, T. G.; Ghobadi, A.; Buyuktemiz, M.; Yildiz, E. A.; Berna Yildiz, D.; Yaglioglu, H. G.; Dede, Y.; Ozbay, E.; Karadas, F. A Robust, Precious- Metal- Free Dye- Sensitized Photoanode for Water Oxidation: A Nanosecond- Long Excited- State Lifetime through a Prussian Blue Analogue. *Angew. Chemie Int. Ed.* **2020**, *59*, 4082–4090.

(39) Zhang, X.; He, J. Co–Fe Prussian Blue Coordination Polymer Modified Silicon Nanowires Array for Efficient Photoelectrochemical Water Oxidation. *J. Nanosci. Nanotechnol.* **2018**, *18*, 5674–5678.

(40) Ma, L.; Chen, S.; Long, C.; Li, X.; Zhao, Y.; Liu, Z.; Huang, Z.; Dong, B.; Zapien, J. A.; Zhi, C. Achieving High- Voltage and High- Capacity Aqueous Rechargeable Zinc Ion Battery by Incorporating Two- Species Redox Reaction. *Adv. Energy Mater.* **2019**, *9*, 1902446.

(41) Lezna, R. O.; Romagnoli, R.; De Tacconi, N. R.; Rajeshwar, K. Cobalt Hexacyanoferrate: Compound Stoichiometry, Infrared Spectroelectrochemistry, and Photoinduced Electron Transfer. *J. Phys. Chem. B* **2002**, *106*, 3612–3621.

(42) Sun, K.; Pang, X.; Shen, S.; Qian, X.; Cheung, J. S.; Wang, D. Metal Oxide Composite Enabled Nanotextured Si Photoanode for Efficient Solar Driven Water Oxidation. *Nano Lett.* **2013**, *13*, 2064–2072.

(43) Moretti, G.; Gervais, C. Raman Spectroscopy of the Photosensitive Pigment Prussian Blue. *J. Raman Spectrosc.* **2018**, *49*, 1198–1204.

(44) *Electrochemical Methods: Fundamentals and Application;* Bard, A. J.; Faulkner, L. R.; John Wiley & Sons, Inc.: New York, 2001.

(45) Qiu, J.; Hajibabaei, H.; R. Nellist, M.; A. L. Laskowski, F.; W. Hamann, T.; W. Boettcher, S. Direct in Situ Measurement of Charge Transfer Processes During Photoelectrochemical Water Oxidation on Catalyzed Hematite. *ACS Cent. Sci.* **2017**, *3*, 1015–1025.

(46) Laskowski, F. A. L.; Nellist, M. R.; Venkatkarthick, R.; Boettcher, S. W. Junction

Behavior of N-Si Photoanodes Protected by Thin Ni Elucidated from Dual Working Electrode Photoelectrochemistry. *Energy Environ. Sci.* **2017**, *10*, 570–579.

(47) Xu, G.; Xu, Z.; Shi, Z.; Pei, L.; Yan, S.; Gu, Z.; Zou, Z. Silicon Photoanodes Partially Covered by Ni@$Ni(OH)_2$ Core-Shell Particles for Photoelectrochemical Water Oxidation. *ChemSusChem* **2017**, *10*, 2897–2903.

(48) Sze, S. M.; Ng, K. K. *Physics of Semiconductor Devices*, 3rd ed.; John Wiley & Sons, Inc.: New Jersey, 2007.

(49) Kenney, M. J.; Gong, M.; Li, Y.; Wu, J. Z.; Feng, J.; Lanza, M.; Dai, H. High-Performance Silicon Photoanodes Passivated with Ultrathin Nickel Films for Water Oxidation. *Science* **2013**, 342, 836–840.

(50) Maruthapandian, V.; Kumaraguru, S.; Mohan, S.; Saraswathy, V.; Muralidharan, S. An Insight on the Electrocatalytic Mechanistic Study of Pristine Ni MOF (BTC) in Alkaline Medium for Enhanced OER and UOR. *ChemElectroChem* **2018**, *5*, 2795–2807.

(51) Wang, Z.; Yang, H.; Gao, B.; Tong, Y.; Zhang, X.; Su, L. Stability Improvement of Prussian Blue in Nonacidic Solutions via an Electrochemical Post-Treatment Method and the Shape Evolution of Prussian Blue from Nanospheres to Nanocubes. *Analyst* **2014**, *139*, 1127.

(52) Salazar, P.; Martín, M.; O'Neill, R. D.; Roche, R.; González-Mora, J. L. Improvement and Characterization of Surfactant-Modified Prussian Blue Screen-Printed Carbon Electrodes for Selective H_2O_2 Detection at Low Applied Potentials. *J. Electroanal. Chem.* **2012**, *674*, 48–56.

(53) Du, J.; Wang, Y.; Zhou, X.; Xue, Z.; Liu, X.; Sun, K.; Lu, X. Improved Sensing in Physiological Buffers by Controlling the Nanostructure of Prussian Blue Films. *J. Phys. Chem. C* **2010**, *114*, 14786–14793.

(54) Medway, S. L.; Lucas, C. A.; Kowal, A.; Nichols, R. J.; Johnson, D. In Situ Studies of the Oxidation of Nickel Electrodes in Alkaline Solution. *J. Electroanal. Chem.* **2006**, *587*, 172–181.

(55) Michael, J. D.; Demeter, E. L.; Illes, S. M.; Fan, Q.; Boes, J. R.; Kitchin, J. R. Alkaline Electrolyte and Fe Impurity Effects on the Performance and Active-Phase Structure of NiOOH Thin Films for OER Catalysis Applications. *J. Phys. Chem. C* **2015**, *119*, 11475–11481.

(56) Vedharathinam, V.; Botte, G. G. Direct Evidence of the Mechanism for the Electro-Oxidation of Urea on $Ni(OH)_2$ Catalyst in Alkaline Medium. *Electrochim. Acta* **2013**, *108*, 660–665.

TOC GRAPHICS